

1 **The effects of different footprint sizes and cloud algorithms on the**
2 **top-of-atmosphere radiative flux calculation from the Clouds and**
3 **Earth's Radiant Energy System (CERES) instrument on Suomi**
4 **National Polar-orbiting Partnership (NPP)**

5 WENYING SU, *

Science Directorate, NASA Langley Research Center, Hampton, Virginia

6 LUSHENG LIANG, WALTER F. MILLER, VICTOR E. SOTHCOTT

Science Systems & Applications, Inc., Hampton, Virginia

* *Corresponding author address:* Wenying Su, MS420, NASA Langley Research Center, Hampton, VA 23681.

E-mail: Wenying.Su-1@nasa.gov

ABSTRACT

7

8 Only one CERES instrument is onboard the Suomi NPP and it has been placed in cross-track
9 mode since launch, it is thus not possible to construct a set of angular distribution models
10 (ADMs) specific for CERES on NPP. Edition 4 Aqua ADMs are used for flux inversions for
11 CERES-NPP measurements. However, the footprint size of CERES-NPP is greater than
12 that of CERES-Aqua, as the altitude of the NPP orbit is higher than that of the Aqua orbit.
13 Furthermore, cloud retrievals from the Visible Infrared Imaging Radiometer Suite (VIIRS)
14 and the Moderate Resolution Imaging Spectroradiometer (MODIS), the imagers sharing the
15 spacecrafts with CERES-NPP and CERES-Aqua, are also different. To quantify the flux
16 uncertainties due to the footprint size difference between CERES-Aqua and CERES-NPP,
17 and due to both the footprint size difference and cloud property difference, a simulation
18 is designed using the MODIS pixel level data which are convolved with the CERES-Aqua
19 and CERES-NPP point spread functions into their respective footprints. The simulation is
20 designed to isolate the effects of footprint size and cloud property differences on flux uncer-
21 tainty from calibration and orbital differences between CERES-NPP and CERES-Aqua. The
22 footprint size difference between CERES-Aqua and CERES-NPP introduces instantaneous
23 flux uncertainties in monthly gridded CERES-NPP of less than 4.0 Wm^{-2} for SW, and less
24 than 1.0 Wm^{-2} for both daytime and nighttime LW. The global monthly mean instanta-
25 neous SW flux from simulated CERES-NPP has a low bias of 0.4 Wm^{-2} when compared
26 to simulated CERES-Aqua, and the root-mean-square (RMS) error is 2.2 Wm^{-2} between
27 them; the biases of daytime and nighttime LW flux are close to zero with RMS errors of 0.8
28 Wm^{-2} and 0.2 Wm^{-2} . These uncertainties are within the uncertainties of CERES ADMs.
29 When both footprint size and cloud property (cloud fraction and optical depth) differences
30 are considered, the uncertainties of monthly gridded CERES-NPP SW flux can be up to
31 20 Wm^{-2} in the Arctic regions where cloud optical depth retrievals from VIIRS differ sig-
32 nificantly from MODIS. The global monthly mean instantaneous SW flux from simulated
33 CERES-NPP has a high bias of 1.1 Wm^{-2} and the RMS error increases to 5.2 Wm^{-2} . LW

34 flux shows less sensitivity to cloud property differences than SW flux, with the uncertainties
35 of about 2 Wm^{-2} in monthly gridded LW flux, and the RMS errors of global monthly mean
36 daytime and nighttime fluxes increase only slightly. These results highlight the importance
37 of consistent cloud retrieval algorithms to maintain the accuracy and stability of the CERES
38 climate data record.

1. Introduction

The Clouds and Earth’s Radiant Energy System (CERES) project has been providing data products crucial to advancing our understanding of the effects of clouds and aerosols on radiative energy within the Earth-atmosphere system. CERES data are used by the science community to study the Earth’s energy balance (e.g., Trenberth et al. 2009; Kato et al. 2011; Loeb et al. 2012; Stephens et al. 2012), aerosol direct radiative effects (e.g., Satheesh and Ramanathan 2000; Zhang et al. 2005; Loeb and Manalo-Smith 2005; Su et al. 2013), aerosol-cloud interactions (e.g., Loeb and Schuster 2008; Quaas et al. 2008; Su et al. 2010b), and to evaluate global general circulation models (e.g., Pincus et al. 2008; Su et al. 2010a; Wang and Su 2013; Wild et al. 2013).

Six CERES instruments have flown on four different satellites thus far. CERES pre-Flight Model (FM) on Tropical Rainfall Measuring Mission (TRMM) was launched on November 27, 1997 into a 350-km circular precessing orbit with a 35° inclination angle and flew together with the Visible and Infrared Scanner (VIRS). CERES instruments (FM1 and FM2) on Terra were launched on December 18, 1999 into a 705-km sun-synchronous orbit with a 10:30 a.m. equatorial crossing time. CERES instruments (FM3 and FM4) on Aqua satellite were launched on May 4, 2002 into a 705-km sun-synchronous orbit with a 1:30 p.m. equatorial crossing time. CERES on Terra and Aqua flies alongside Moderate-Resolution Imaging Spectroradiometer (MODIS). CERES instrument (FM5) was launched onboard Suomi NPP (hereafter referred to as NPP) on October 28, 2011 into a 824-km sun-synchronous orbit with a 1:30 p.m. equatorial crossing time and flies alongside the Visible Infrared Imaging Radiometer Suite (VIIRS). As the orbit altitudes differ among these satellites, the spatial resolutions of CERES instruments also vary from each other. TRMM has the lowest orbit altitude and offers the highest spatial resolution of CERES measurements, about 10 km at nadir; the spatial resolution of CERES on Terra and Aqua is about 20 km at nadir; and is about 24 km at nadir for NPP as it has the highest orbit altitude.

The CERES instrument consists of a three-channel broadband scanning radiometer (Wielicki

66 et al. 1996). The scanning radiometer measures radiances in shortwave (SW, 0.3-5 μm), win-
 67 dow (WN, 8-12 μm), and total (0.3-200 μm) channels. The longwave (LW) component is
 68 derived as the difference between total and SW channels. These measured radiances (I) at
 69 a given sun-Earth-satellite geometry are converted to outgoing reflected solar and emitted
 70 thermal TOA radiative fluxes (F) as:

$$F(\theta_0) = \frac{\pi I(\theta_0, \theta, \phi)}{R_j(\theta_0, \theta, \phi)}. \quad (1)$$

71 where θ_0 is the solar zenith angle, θ is the CERES viewing zenith angle, ϕ is the relative
 72 azimuth angle between CERES and the solar plane, and $R_j(\theta_0, \theta, \phi)$ is the anisotropic factors
 73 for scene type j . Here scene type is a combination of variables (e.g., surface type, cloud
 74 fraction, cloud optical depth, cloud phase, aerosol optical depth, precipitable water, lapse
 75 rate, etc) that are used to group the data to develop distinct angular distribution models
 76 (ADMs). Note the SW ADMs are developed as a function of θ_0, θ, ϕ for each scene type,
 77 whereas the LW ADMs are a weak function of θ_0 and ϕ and are developed only as a function
 78 of θ (Loeb et al. 2005; Su et al. 2015a).

79 To facilitate the construction of ADMs, there are pairs of identical CERES instruments
 80 on both Terra and Aqua. At the beginning of these missions one of the instruments on each
 81 satellite was always placed in a rotating azimuth plane (RAP) scan mode, while the other
 82 one was placed in cross-track mode to provide spatial coverage. When in RAP mode, the
 83 instrument scans in elevation as it rotates in azimuth, thus acquiring radiance measurements
 84 from a wide range of viewing combinations. There are about 60 months of RAP data collected
 85 on Terra and about 32 months of RAP data collected on Aqua. CERES instruments fly
 86 alongside high-resolution imagers, which provide accurate scene type information within
 87 the CERES footprints. Cloud and aerosol retrievals based upon high-resolution imager
 88 measurements are averaged over the CERES footprints by accounting for the CERES point
 89 spread function (PSF, Smith 1994) and are used for scene type classification. Similarly,
 90 spectral radiances from MODIS/VIIRS observations are averaged over the CERES footprints
 91 weighted by the CERES PSF. Surface types are obtained from the International Geosphere

92 Biosphere Program (IGBP, Loveland and Belward 1997) global land cover data set. Fresh
93 snow and sea ice surface types are derived from a combination of the National Snow and Ice
94 Data Center (NSIDC) microwave snow/ice map and the National Environmental Satellite,
95 Data and Information Service (NESDIS) snow/ice map. NESDIS uses imager data to identify
96 snow and sea ice and provide snow and sea ice information near the coast, whereas NSIDC
97 does not provide microwave retrievals within 50 km of the coast.

98 TRMM ADMs were developed using 9 months of CERES observations and the scene
99 identification information retrieved from VIRS observations (Loeb et al. 2003). Terra ADMs
100 and Aqua ADMs were developed separately using multi-year CERES Terra and Aqua mea-
101 surements in RAP mode and in cross-track mode using the scene identification information
102 from Terra MODIS and Aqua MODIS (Loeb et al. 2005; Su et al. 2015a). The high-resolution
103 MODIS imager provides cloud conditions for every CERES footprint. The cloud algorithms
104 developed by the CERES cloud working group retrieve cloud fraction, cloud optical depth,
105 cloud phase, cloud top and effective temperature/pressure (among other variables) based on
106 MODIS pixel-level measurements (Minnis et al. 2010). These pixel-level cloud properties
107 are spatially and temporally matched with the CERES footprints and are used to select the
108 scene-dependent ADMs to convert the CERES measured radiances to fluxes (Eq.1). The
109 spatial matching criterion used is 1 km. The temporal matching criterion used is less than
110 20 seconds when CERES is in cross-track mode, and less than 6 minutes when CERES is in
111 RAP mode.

112 There is only one CERES instrument on NPP and it has been placed in cross-track scan
113 mode since launch, it is thus not feasible to develop a specific set of ADMs for CERES
114 on NPP. Currently, the Edition 4 Aqua ADMs (Su et al. 2015a) are used to invert fluxes
115 for the CERES measurements on NPP. The CERES footprint size on NPP is larger than
116 that on Aqua. As pointed out by Di Girolamo et al. (1998), the nonreciprocal behavior
117 of the radiation field depends on measurement resolution, which means the ADMs do too.
118 They concluded that ADMs should be applied only to data of the same resolution as the

119 data used to derive the ADMs. Since the footprint sizes are different between CERES-Aqua
120 and CERES-NPP, will using ADMs developed based upon CERES-Aqua measurements for
121 CERES-NPP flux inversion introduce any uncertainties in the CERES-NPP flux? Addition-
122 ally, ADMs are scene type dependent, it is important to use consistent scene identification
123 for developing and applying the ADMs. However, the VIIRS channels are not identical to
124 those of MODIS, especially the lack of $6.7 \mu\text{m}$ and $13.3 \mu\text{m}$ channels, caused the cloud prop-
125 erties retrieved from MODIS and VIIRS differ from each other. These differences affect the
126 scene identification used to select the ADMs for flux inversion and thus can lead to addi-
127 tional uncertainties in the CERES-NPP flux. In this study, we design a simulation study to
128 quantify the CERES-NPP flux uncertainties due to the footprint size difference alone, and
129 due to both the footprint size and cloud property differences.

130 **2. Comparison between CERES-Aqua and CERES-NPP**

131 Besides the altitude differences between Aqua and NPP satellites, they are also different
132 in other orbital characteristics. For example, the orbital period for Aqua is about 98.82
133 minutes, while it is about 101.44 minutes for NPP; and the orbital inclination for Aqua is
134 about 98.20° , while it is about 98.75° for NPP. These orbital differences result in different
135 local overpass times between Aqua and NPP and their orbits fly over each other about every
136 64 hours. These simultaneous observations from Aqua and NPP are matched to compare
137 SW and LW radiances using CERES Aqua Edition 4 Single Scanner Footprint TOA/Surface
138 Fluxes and Clouds (SSF) product and CERES NPP Edition 1 SSF product. Here we use I_a^m
139 to denote the CERES-Aqua (subscript a) measured (superscript m) radiance, and I_n^m as the
140 CERES-NPP (subscript n) measured radiance. Similarly, F_a^m and F_n^m are the fluxes derived
141 from I_a^m and I_n^m using CERES Aqua ADMs. The matching criteria used for SW radiances
142 are that the latitude and longitude differences between the Aqua footprints and the NPP
143 footprints are less than 0.05 degree, solar zenith angle and viewing zenith angle differences

144 are less than 2 degrees, and relative azimuth angle difference is less than 5 degrees. The
145 matching criteria used here also provide a tight constraint on scattering angles, with about
146 95.6% and 99.9% of the matched footprints having scattering angle differences less than 2
147 degrees and 3 degrees, respectively. Same latitude and longitude matching criteria are used
148 for LW radiances and the viewing zenith angle difference between the Aqua footprints and
149 the NPP footprints is less than 2 degrees.

150 Figure 1 shows the SW, daytime LW, and nighttime LW radiance comparisons between
151 CERES-Aqua and CERES-NPP using matched footprints of 2013 and 2014. The total
152 number of matched footprints, the mean I_a^m and I_n^m , and the root-mean-square (RMS) errors
153 are summarized in Table 1. The mean SW I_n^m is about $1 \text{ Wm}^{-2}\text{sr}^{-1}$ greater than I_a^m , the mean
154 daytime LW I_n^m is about $0.4 \text{ Wm}^{-2}\text{sr}^{-1}$ smaller than I_a^m , and the nighttime LW I_n^m and I_a^m
155 agree to within $0.1 \text{ Wm}^{-2}\text{sr}^{-1}$. Excluding matched footprints with scattering angle difference
156 greater than 2 degrees does not change the SW comparison result. These comparisons
157 include data taken from nadir to oblique viewing angles ($\theta > 60$). The RMS errors remain
158 almost the same when we compare the radiances taken at different θ ranges. Footprint size
159 differences may also contribute to the radiance differences, but these radiance differences
160 should be random. It is likely that the footprint size differences can increase the RMS errors,
161 but the mean radiance differences are mostly resulted from calibration differences between
162 CERES-Aqua and CERES-NPP. As mentioned earlier, the daytime CERES LW radiance
163 is derived as the difference between total channel and SW channel measurements, and the
164 nighttime CERES LW radiance is directly derived from the total channel measurements.
165 The differences shown in Table 1 indicate that the agreement of the total channels between
166 CERES-Aqua and CERES-NPP are better than that of the SW channels, leading to a smaller
167 daytime LW difference than SW difference. Loeb et al. (2016) examined the normalized
168 instrument gains for the total and SW channels for CERES FM1-FM5 since the beginning
169 of the mission (BOM). The total channel response to LW radiation has gradually increased
170 with time for all instruments. For the two instruments (FM3 and FM5) that are of interest

171 here, the increases relative to the BOM are 0.7% for FM3 and 0.4% for FM5. The SW
172 channel response increases about 0.4% for FM3 and decreases by 0.2% for FM5. Exact
173 causes for the calibration differences between CERES-Aqua and CERES-NPP are not yet
174 known and more research are needed to understand their differences. The future plan is to
175 place CERES-NPP on the same radiometric scale as CERES-Aqua.

176 Flux comparison using the same matched footprints are shown in Figure 2 and the mean
177 F_a^m and F_n^m , and the RMS errors between them are summarized in Table 1. Consistent with
178 the radiance comparisons, the mean SW F_n^m is about 3.8 Wm^{-2} greater than F_a^m , the mean
179 daytime LW F_n^m is about 1.0 Wm^{-2} smaller than F_a^m , and the mean nighttime LW F_n^m is
180 about 0.3 Wm^{-2} smaller than F_a^m . When we compare the relative RMS errors (RMS error
181 divided by the mean Aqua value) between radiance and flux, the relative flux RMS errors
182 (6.4% for SW, 2.2% for daytime LW, and 1.4% for nighttime LW) are always slightly larger
183 than the relative radiance RMS errors (6.0% for SW, 2.1% for daytime LW, and 1.1% for
184 nighttime LW). This indicates that additional uncertainties are added when the radiances
185 are converted to fluxes.

186 However, we cannot directly compare the gridded monthly mean fluxes from Aqua and
187 NPP as their overpass times differ. Figure 3 shows the monthly mean TOA insolation differ-
188 ence between CERES-NPP and CERES-Aqua for April 2013. Insolation for NPP overpass
189 times is greater than that for Aqua overpass times over most regions, except over the northern
190 high latitude where NPP has significantly more overpasses at $\theta_0 > 70^\circ$ than Aqua. Regional
191 differences as large as 30 Wm^{-2} are observed over the tropical regions and north of 60°N .
192 Globally, the CERES-NPP monthly mean insolation is greater than that of CERES-Aqua by
193 13.4 Wm^{-2} for this month. When we compare the monthly gridded TOA reflected SW flux
194 between CERES-NPP and CERES-Aqua (Figure 4a), the difference features in high latitude
195 regions (north of 60°N and south of 60°S) resemble those of the insolation differences. We
196 then compare the albedo between CERES-NPP and CERES-Aqua (Figure 4b). Over most
197 regions, the albedo from CERES-NPP is greater than that from CERES-Aqua, except over

198 parts of tropical oceans and Antarctica where some negative differences are observed. The
199 global monthly mean albedo from CERES-NPP is greater than that from CERES-Aqua by
200 0.003 (1.02%). The albedo difference is mostly from the calibration differences (see Figure
201 1a and Table 1), while the footprint size difference and scene identification difference also
202 contribute to the albedo difference.

203 The CERES cloud working group developed sophisticated cloud detection algorithms
204 using visible and infrared channels of MODIS separately for polar and non-polar regions
205 and for daytime, twilight, and nighttime (Trepte et al. 2010). However, these detection
206 algorithms have to be modified to be applicable to the VIIRS observations (Qing Trepte,
207 personal communication), as some of the MODIS channels utilized for cloud detection are
208 not available on VIIRS. These modifications include replacing the 2.1 μm MODIS channel
209 with the 1.6 μm VIIRS channel, and replacing detection tests using MODIS 6.7 μm and 13.3
210 μm channels with VIIRS 3.7 μm and 11 μm channels, and supplement with tests utilizing
211 VIIRS 1.6 μm channel and the brightness temperature differences between 11 μm and 12 μm .
212 These changes mainly affect cloud detections over the polar regions. The parameterization
213 of 1.24 μm reflectance was regenerated for VIIRS using improved wavelength and insolation
214 weighting, which affects cloud optical depth retrieval over the snow/ice surfaces (Szedung
215 Sun-Mack, personal communication). These changes result in different cloud properties
216 retrieved using MODIS and VIIRS, especially over the polar regions. Figure 5 shows the
217 daytime cloud fraction and cloud optical depth difference between VIIRS and Aqua-MODIS
218 for April 2013. Cloud fraction retrieved from VIIRS is greater than that from MODIS by
219 up to 10% and cloud optical depth from VIIRS is smaller than that from MODIS by 2~3
220 over part of the Antarctic. Cloud fraction from VIIRS over the northern high-latitude snow
221 regions is smaller than that from MODIS, while the optical depth from VIIRS is greater
222 than that from MODIS. Over the Arctic, cloud optical depth from VIIRS is much larger
223 than that from MODIS. Over the ocean between 60°S and 60°N, the differences in cloud
224 fraction seem rather random while the differences in cloud optical depth is mostly positive

225 (VIIRS retrieval is greater than Aqua-MODIS retrieval).

226 Given that the footprint sizes and overpass times are different between CERES-Aqua
227 and CERES-NPP, in addition to the calibration differences and cloud retrieval differences
228 between them, fluxes from these CERES instruments cannot be compared directly to assess
229 the effects of footprint size difference and cloud property difference on flux uncertainty.

230 **3. Method**

231 To quantify the footprint size and cloud retrieval effect on flux inversion without having
232 to account for the calibration and overpass time differences, we design a simulation study
233 using the MODIS pixel level data and the Aqua-Earth-Sun geometry. MODIS spectral
234 measurements are used to retrieve cloud properties and aerosol optical depth. These pixel-
235 level imager-derived aerosol and cloud properties, and spectral narrowband (NB) radiances
236 from MODIS are convolved with the CERES PSF to provide the most accurate aerosol and
237 cloud properties that are spatially and temporally matched with the CERES broadband
238 radiance data. Figure 6 illustrates the process of generating the simulated CERES-Aqua
239 and CERES-NPP footprints from the MODIS pixels. We first use the CERES-Aqua PSF
240 to convolve the aerosol/cloud properties, and the MODIS NB radiances (and other ancillary
241 data) into Aqua-size footprints (left portion of Figure 6), as is done for the standard CERES-
242 Aqua SSF product. These NB radiances for the simulated CERES-Aqua footprints are
243 denoted as $I_a^s(\lambda)$, where superscript ‘s’ is for the simulated (in contrast to superscript ‘m’
244 for the measured). We then increase the footprint size to be that of NPP and use the
245 CERES-NPP PSF to average the MODIS NB radiances, cloud/aerosol properties, and other
246 ancillary data into the simulated NPP footprints. NB radiances for the simulated CERES-
247 NPP footprints are denoted as $I_n^s(\lambda)$.

248 Four months (July 2012, October 2012, January 2013, and April 2013) of simulated
249 CERES-Aqua and CERES-NPP data were created. For every CERES-Aqua footprint, it

250 contains the broadband SW and LW radiances measured by the CERES instrument. The
251 simulated NPP footprints, however, do not contain broadband radiances. To circumvent
252 this issue, we developed narrowband-to-broadband coefficients to convert the MODIS NB
253 radiances to broadband radiances.

254 The Edition 4 CERES-Aqua SSF data from July 2002 to September 2007 are used to
255 derive the narrowband-to-broadband (NB2BB) regression coefficients separately for SW,
256 daytime LW, and nighttime LW. Seven MODIS spectral bands (0.47, 0.55, 0.65, 0.86, 1.24,
257 2.13, and 3.7 μm) are used to derive the broadband SW radiances, and the SW regression
258 coefficients are calculated for every calendar month for discrete intervals of solar zenith angle,
259 viewing zenith angle, relative azimuth angle, surface type, snow/non-snow conditions, cloud
260 fraction, and cloud optical depth. Five MODIS spectral bands (6.7, 8.5, 11.0, 12.0, and 14.2
261 μm) are used to derive the broadband LW radiances, and the LW regression coefficients are
262 calculated for every calendar month for discrete intervals of viewing zenith angle, precipitable
263 water, surface type, snow/none-snow conditions, cloud fraction, and cloud optical depth. The
264 20 IGBP surface types are grouped into 8 surface types: ocean, forest, savanna, grassland,
265 dark desert, bright desert, the Greenland permanent snow, and the Antarctic permanent
266 snow. When there is sea ice over the ocean and snow over the land surface types, regression
267 coefficients for ice and snow conditions are developed (only footprints with 100% sea ice/snow
268 coverage are considered).

269 These SW and LW NB2BB regression coefficients are then applied to $I_a^s(\lambda)$ and $I_n^s(\lambda)$
270 to derive the broadband radiances, I_a^s and I_n^s , for simulated footprints of CERES-Aqua
271 and CERES-NPP, shown on the left and right of Figure 6, if the footprint consists of a
272 single surface type. As both simulated CERES-Aqua and CERES-NPP footprints use the
273 Aqua-Earth-Sun geometry, I_a^s and I_n^s have the same Sun-viewing geometry. Even though the
274 CERES-Aqua footprints contained the broadband radiances from CERES observations (I_a^m),
275 we choose to use the broadband radiances calculated using the NB2BB regressions to ensure
276 that I_a^s and I_n^s are consistently derived. Doing so we can isolate the flux differences between

277 simulated CERES-Aqua and simulated CERES-NPP caused by footprint size difference.

278 The cloud properties in the simulated CERES-Aqua footprints and in the simulated
279 CERES-NPP footprints are all based upon the MODIS retrievals, so the scene identifica-
280 tions used to select ADMs for flux inversion are almost the same for both the simulated
281 CERES-Aqua and the CERES-NPP, except for small differences due to differing footprint
282 sizes. As demonstrated in Figure 5, cloud properties differ between the MODIS and the VI-
283 IRS retrievals. These cloud retrieval differences affect the anisotropy factors selected for flux
284 inversion. To simulate both the footprint size and cloud property differences, cloud fraction
285 and cloud optical depth retrievals from MODIS convolved in the simulated CERES-NPP
286 footprints are adjusted to be similar to those from VIIRS retrievals to assess how cloud
287 retrieval differences affect the flux. To accomplish this, daily cloud fraction ratios of VIIRS
288 to MODIS are calculated for each 1° latitude by 1° longitude grid box. These ratios are then
289 applied to the cloudy footprints of MODIS retrieval to adjust the MODIS cloud fractions
290 to be nearly the same as those from VIIRS retrieval. Note no adjustment is done for clear
291 footprints. Similarly, daily cloud optical depth ratios of VIIRS to MODIS are calculated us-
292 ing cloudy footprints for each 1° by 1° grid box. These ratios are used to adjust the MODIS
293 retrieved cloud optical depth to be close to those from VIIRS retrievals. The process of gen-
294 erating the simulated CERES-NPP footprints with VIIRS-like cloud retrievals is illustrated
295 on the lower right portion of Figure 6.

296 Aqua ADMs are then used to convert I_a^s and I_n^s to fluxes, F_a^s and F_n^s , for the simulated
297 CERES-Aqua and CERES-NPP footprints using the cloud properties retrieved from MODIS
298 observations for scene type identification. To further access the effects of both footprint size
299 and cloud property differences on flux inversion, Aqua ADMs are used to convert I_n^s to flux,
300 $F_n'^s$, for the simulated CERES-NPP footprints using VIIRS-like cloud properties for scene
301 identification.

4. Results

We first compare the footprint-level fluxes between simulated CERES-Aqua and simulated CERES-NPP using data of April 1, 2013 (about 700,000 footprints). As the cloud fraction and cloud optical depth adjustments are done at the grid box level, it is not feasible to compare footprint-level $F'_n{}^s$ and $F_n{}^s$, and only footprint-level $F'_a{}^s$ and $F_a{}^s$ are compared. For SW, the bias between $F'_a{}^s$ and $F_a{}^s$ is 0.1 Wm^{-2} and the RMS error is 4.7 Wm^{-2} . For LW, the biases is close to zero and the RMS errors are 1.3 Wm^{-2} and 0.9 Wm^{-2} for daytime and nighttime, respectively. These flux RMS errors are much smaller than those listed in Table 1, indicating that calibration differences are responsible for most of the flux differences between CERES-Aqua and CERES-NPP measurements. However, we should avoid direct comparisons between these two sets of RMS errors, as they are derived using different time period.

We now compare the monthly grid box (1° latitude by 1° longitude) mean fluxes from the three simulations outlined in the previous section. Differences between $F'_n{}^s$ and $F_a{}^s$ are used to assess the CERES-NPP gridded monthly mean instantaneous flux uncertainties due to the footprint size difference, and differences between $F'_n{}^s$ and $F'_a{}^s$ are used to assess the CERES-NPP gridded monthly mean instantaneous flux uncertainties due to both the footprint size and cloud property differences.

The monthly mean instantaneous TOA SW fluxes for simulated CERES-Aqua ($F_a{}^s$) are shown in Figure 7(a) for April 2013. Note these fluxes are different from those in the Edition 4 Aqua SSF product as the CERES measured radiances differ from those inferred using NB2BB regression coefficients. The flux differences caused by the footprint size difference between the simulated CERES-NPP and the simulated CERES-Aqua ($F'_n{}^s - F_a{}^s$) are shown in Figure 7(b). Grid boxes in white indicate that the number of footprints with valid SW fluxes differ by more than 2% between simulated CERES-Aqua and CERES-NPP, as the NB2BB regressions are only applied to footprints that consist of the same surface types which result in fewer footprints with valid fluxes for CERES-NPP than for CERES-Aqua. The

329 footprint size difference between CERES-Aqua and CERES-NPP introduces an uncertainty
330 that rarely exceeds 4.0 Wm^{-2} in monthly gridded CERES-NPP instantaneous SW fluxes.
331 For global monthly mean instantaneous SW flux, the simulated CERES-NPP has a low bias
332 of 0.4 Wm^{-2} compares to the simulated CERES-Aqua, and the RMS error between them is
333 2.4 Wm^{-2} . Results from the other three months are very similar to April 2013 (not shown).

334 Figure 7(c) shows the SW flux difference caused by both the footprint size and cloud prop-
335 erty differences ($F_n^{s'} - F_a^s$). Adding the cloud property differences increase the CERES-NPP
336 flux uncertainty comparing to when only footprint size differences are considered (Figure
337 7(b)), monthly gridded instantaneous flux uncertainty over the Arctic ocean can exceed 20
338 Wm^{-2} . Accounting for cloud property differences, the global monthly mean instantaneous
339 SW flux from simulated CERES-NPP has a high bias of 1.1 Wm^{-2} and the RMS error is
340 increased to 5.2 Wm^{-2} . Over the Arctic Ocean, the cloud optical depth from VIIRS retrieval
341 is much greater than that from the MODIS retrieval while the difference in cloud fraction is
342 relatively small. Anisotropic factors for thick clouds are smaller than those for thin clouds
343 at oblique viewing angles, and are larger for near-nadir viewing angles. The viewing ge-
344 ometries over the Arctic Ocean produced more smaller anisotropic factors than larger ones
345 when MODIS cloud optical depths were replaced with VIIRS-like cloud optical depths, which
346 resulted in larger fluxes when using VIIRS-like cloud properties for flux inversion.

347 The daytime and nighttime LW flux from the simulated CERES-Aqua footprints, LW
348 flux differences due to footprint size difference, and LW flux difference due to both footprint
349 size difference and cloud property difference are shown in Figures 8 and 9. The effect of
350 footprint size on gridded monthly mean daytime and nighttime LW flux is generally within
351 1.0 Wm^{-2} . For global monthly mean LW flux, the differences between $F_n^s - F_a^s$ are close to
352 zero, and the RMS errors between them are about 0.8 Wm^{-2} and 0.2 Wm^{-2} for daytime
353 and nighttime LW fluxes. When cloud property differences are also considered, their effect
354 on gridded monthly mean LW fluxes increases to about 2 Wm^{-2} . The RMS errors of global
355 monthly mean LW flux increase slightly to about 0.9 Wm^{-2} and 0.5 Wm^{-2} for daytime and

356 nighttime. The LW fluxes showed much less sensitivity to cloud property changes than the
357 SW fluxes, especially over the Arctic Ocean where cloud optical depth changed significantly.
358 This is because the LW ADMs over the snow/ice surfaces have very little sensitivity to cloud
359 optical depth (Su et al. 2015a), but they were developed for discrete cloud fraction intervals
360 and larger flux changes are noted in regions experiencing large cloud fraction changes.

361 5. Summary and discussion

362 The scene-type dependent ADMs are used to convert the radiances measured by the
363 CERES instruments to fluxes. Specific empirical ADMs were developed for CERES instru-
364 ments on TRMM, Terra, and Aqua (Loeb et al. 2003, 2005; Su et al. 2015a). As there is only
365 one CERES instrument on NPP and it has been placed in cross-track mode since launch,
366 it is not possible to construct a set of ADMs specific for CERES on NPP. Edition 4 Aqua
367 ADMs (Su et al. 2015a) are thus used for flux inversions for CERES-NPP measurements.
368 However, the altitude of the NPP orbit is higher than that of the Aqua orbit resulting in
369 a larger CERES footprint size on NPP than on Aqua. Given that the footprint size of
370 CERES-NPP is different from that of CERES-Aqua, we need to quantify the CERES-NPP
371 flux uncertainty caused by using the CERES-Aqua ADMs. Furthermore, there are some
372 differences between the imagers that are on the same spacecrafts as CERES-Aqua (MODIS)
373 and CERES-NPP (VIIRS), as VIIRS lacks the $6.7 \mu\text{m}$ and $13.3 \mu\text{m}$ channels. These spectral
374 differences and algorithm differences lead to notable cloud fraction and cloud optical depth
375 differences retrieved from MODIS and VIIRS. As the anisotropy factors are scene-type de-
376 pendent, differences in cloud properties will also introduce uncertainties in flux inversion.
377 Furthermore, the calibrations between CERES instruments on Aqua and on NPP also are
378 different from each other. Comparisons using two years of collocated CERES-Aqua and
379 CERES-NPP footprints indicate that the SW radiances from CERES-NPP are about 1.5%
380 greater than those from CERES-Aqua, the daytime LW radiances from CERES-NPP are

381 about 0.5% smaller than those from CERES-Aqua, and the nighttime LW radiances agree
382 to within 0.1%.

383 To quantify the flux uncertainties due to the footprint size difference between CERES-
384 Aqua and CERES-NPP, and due to both the footprint size difference and cloud property
385 difference, we use the MODIS pixel level data to simulate the CERES-Aqua and CERES-
386 NPP footprints. The simulation is designed to isolate the effects of footprint size differ-
387 ence and cloud property difference on flux uncertainty from calibration difference between
388 CERES-NPP and CERES-Aqua. The pixel-level MODIS spectral radiances, the imager-
389 derived aerosol and cloud properties, and other ancillary data are first convolved with the
390 CERES Aqua PSF to generate the simulated CERES-Aqua footprints, and then convolved
391 with the CERES NPP PSF to generate the simulated CERES-NPP footprints. Broadband
392 radiances within the simulated CERES-Aqua and CERES-NPP footprints are derived us-
393 ing the MODIS spectral bands based upon narrowband-to-broadband regression coefficients
394 developed using five years of Aqua data to ensure consistency between broadband radi-
395 ances from simulated CERES-Aqua and CERES-NPP. These radiances are then converted
396 to fluxes using the CERES-Aqua ADMs. The footprint size difference between CERES-Aqua
397 and CERES-NPP introduces instantaneous flux uncertainties in monthly gridded CERES-
398 NPP of less than 4.0 Wm^{-2} for SW, and less than 1.0 Wm^{-2} for both daytime and nighttime
399 LW. The global monthly mean instantaneous SW flux from simulated CERES-NPP has a
400 low bias of 0.4 Wm^{-2} compares to that from simulated CERES-Aqua, and the RMS error
401 between them is 2.4 Wm^{-2} . The biases in global monthly mean LW fluxes are close to zero,
402 and the RMS errors between simulated CERES-NPP and simulated CERES-Aqua are about
403 0.8 Wm^{-2} and 0.2 Wm^{-2} for daytime and nighttime global monthly mean LW fluxes.

404 The cloud properties in the simulated CERES-Aqua footprints and in the simulated
405 CERES-NPP footprints are all based upon MODIS retrievals, but in reality cloud prop-
406 erties retrieved from VIIRS differ from those from MODIS. To assess the flux uncertainty
407 from scene identification differences, cloud fraction and cloud optical depth in the simulated

408 CERES-NPP footprints are perturbed to be more like the VIIRS retrievals. When both
409 footprint size and cloud property differences are considered, the uncertainties of monthly
410 gridded CERES-NPP SW flux can be up to 20 Wm^{-2} in the Arctic regions where cloud
411 optical depth retrievals from VIIRS differ significantly from MODIS. The global monthly
412 mean instantaneous SW flux from simulated CERES-NPP has a high bias of 1.1 Wm^{-2} and
413 the RMS error is increased to 5.2 Wm^{-2} . LW flux shows less sensitivity to cloud property
414 differences than SW flux, with the uncertainties of about 2.0 Wm^{-2} in monthly gridded LW
415 flux, and the RMS errors increases to 0.9 Wm^{-2} and 0.5 Wm^{-2} for daytime and nighttime
416 LW flux.

417 Su et al. (2015b) quantified the global monthly 24hr-averaged flux uncertainties due to
418 CERES ADMs using direct integration tests, and concluded that the RMS errors are less
419 than 1.1 Wm^{-2} and 0.8 Wm^{-2} for 24hr-averaged TOA SW and LW fluxes. The uncertainty
420 for global monthly instantaneous SW flux is approximately twice the uncertainty of 24hr-
421 averaged flux. This simulation study indicates that the footprint size differences between
422 CERES-NPP and CERES-Aqua introduce flux uncertainties that are within the uncertain-
423 ties of the CERES ADMs. However, the uncertainty assessment provided here should be
424 considered as the low end, as many regions (especially over land, snow, and ice) were not
425 included due to sample number differences within the grid boxes. When cloud property
426 differences are accounted for, the SW flux uncertainties increase significantly and exceed the
427 uncertainties of the CERES ADMs. These findings indicate that inverting CERES-NPP flux
428 using CERES-Aqua ADMs resulting in flux uncertainties that are within the ADMs uncer-
429 tainties as long as the cloud retrievals between VIIRS and MODIS are consistent. When
430 the cloud retrieval differences between VIIRS and MODIS are accounted for, the SW flux
431 uncertainties exceed those of the CERES ADMs. To maintain the consistency of the CERES
432 climate data record, it is thus important to develop cloud retrieval algorithms that account
433 for the capabilities of both MODIS and VIIRS to ensure consistent cloud properties from
434 both imagers.

436 *Acknowledgments.*

437 This research was supported by the NASA CERES project. The CERES data were ob-
438 tained from the NASA Langley Atmospheric Science Data Center at [https://eosweb.larc.nasa.](https://eosweb.larc.nasa.gov/project/ceres/ssf_table)
439 [gov/project/ceres/ssf_table](https://eosweb.larc.nasa.gov/project/ceres/ssf_table). We thank Norman Loeb, Szedung Sun-Mack, Qing Treppe, and
440 Patrick Minnis for helpful discussions, and the three reviewers for their constructive com-
441 ments and suggestions which have significantly improved this paper.

REFERENCES

- 444 Di Girolamo, L., T. Varnai, and R. Davies, 1998: Apparent breakdown of reciprocity in
445 reflected solar radiances. *J. Geophys. Res.*, **103 (D8)**, 8795–8803.
- 446 Kato, S., et al., 2011: Improvements of top-of-atmosphere and surface irradiance computa-
447 tion with CALIPSO-, and MODIS-derived cloud and aerosol properties. *J. Geophys. Res.*,
448 **116 (D19209)**, D19 209, doi:10.1029/2011JD016050.
- 449 Loeb, N. G., S. Kato, K. Loukachine, and N. Manalo-Smith, 2005: Angular distribution
450 models for top-of-atmosphere radiative flux estimation from the clouds and the earth’s
451 radiant energy system instrument on the terra satellite. part I: Methodology. *J. Atmos.*
452 *Oceanic Technol.*, **22**, 338–351.
- 453 Loeb, N. G., J. M. Lyman, G. C. Johnson, R. P. Allan, D. R. Doelling, T. Wong, B. J.
454 Soden, and G. L. Stephens, 2012: Observed changes in top-of-the-atmosphere radiation
455 and upper-ocean heating consistent within uncertainty. *Nature Geosci.*, **5**, 110–113, doi:
456 10.1038/NGEO1375.
- 457 Loeb, N. G. and N. Manalo-Smith, 2005: Top-of-atmosphere direct radiative effect of aerosols
458 over global oceans from merged CERES and MODIS observations. *J. Climate*, **18**, 3506–
459 3526.
- 460 Loeb, N. G., N. Manalo-Smith, S. Kato, W. F. Miller, S. K. Gupta, P. Minnis, and B. A.
461 Wielicki, 2003: Angular distribution models for top-of-atmosphere radiative flux estima-
462 tion from the Clouds and the Earth’s Radiant Energy System instrument on the Tropical
463 Rainfall Measuring Mission satellite. Part I: Methodology. *J. Appl. Meteor.*, **42**, 240–265.

- 464 Loeb, N. G., N. Manalo-Smith, W. Su, M. Shankar, and S. Thomas, 2016: CERES top-of-
465 atmosphere Earth radiation budget climate data record: Accounting for in-orbit changes
466 in instrument calibration. *Remote Sens.*, **8 (182)**, doi:10.3390/rs8030182.
- 467 Loeb, N. G. and G. L. Schuster, 2008: An observational study of the relationship between
468 cloud, aerosol and meteorology in broken low-level cloud conditions. *J. Geophys. Res.*,
469 **113 (D14214)**, D14 214, doi:10.1029/2007JD009763.
- 470 Loveland, T. R. and A. S. Belward, 1997: The international geosphere biosphere programme
471 data and information system global land cover dataset (DISCover). *Acta Astronaut.*, **41**,
472 681–689.
- 473 Minnis, P., et al., 2010: CERES Edition 3 cloud retrievals. *13th Conference on Atmospheric*
474 *Radiation*, Am. Meteorol. Soc., Oregon, Portland.
- 475 Pincus, R., C. P. Batstone, R. J. P. Hofmann, K. E. Taylor, and P. J. Glecker, 2008: Evalu-
476 ating the present-day simulation of clouds, precipitation, and radiation in climate models.
477 *J. Geophys. Res.*, **113 (D14209)**, D14 209, doi:10.1029/2007JD009334.
- 478 Quaas, J., O. Boucher, N. Bellouin, and S. Kinne, 2008: Satellite-based estimate of the
479 direct and indirect aerosol climate forcing. *J. Geophys. Res.*, **113 (D05204)**, D05 204,
480 doi:10.1029/2007JD008962.
- 481 Satheesh, S. K. and V. Ramanathan, 2000: Large differences in tropical aerosol forcing at
482 the top of the atmosphere and earth’s surface. *Nature*, **405**, 60–63.
- 483 Smith, G. L., 1994: Effects of time response on the point spread function of a scanning
484 radiometer. *Appl. Opt.*, **33**, 7031–7037.
- 485 Stephens, G. L., et al., 2012: An update on Earth’s energy balance in light of the latest
486 global observations. *Nature Geosci.*, **5**, 691–696, doi:10.1038/NGEO1580.

487 Su, W., A. Bodas-Salcedo, K.-M. Xu, and T. P. Charlock, 2010a: Comparison of the trop-
488 ical radiative flux and cloud radiative effect profiles in a climate model with Clouds and
489 the Earth’s Radiant Energy System (CERES) data. *J. Geophys. Res.*, **115** (D01105),
490 D01 105, doi:10.1029/2009JD012490.

491 Su, W., J. Corbett, Z. A. Eitzen, and L. Liang, 2015a: Next-generation angular distribution
492 models for top-of-atmosphere radiative flux calculation from the CERES instruments:
493 Methodology. *Atmos. Meas. Tech.*, **8**, 611–632, doi:10.5194/amt-8-611-2015.

494 Su, W., J. Corbett, Z. A. Eitzen, and L. Liang, 2015b: Next-generation angular distribution
495 models for top-of-atmosphere radiative flux calculation from the CERES instruments:
496 Validation. *Atmos. Meas. Tech.*, **8**, 3297–3313, doi:10.5194/amt-8-3297-2015.

497 Su, W., N. G. Loeb, G. L. Schuster, M. Chin, and F. G. Rose, 2013: Global all-sky shortwave
498 direct radiative forcing of anthropogenic aerosols from combined satellite observations and
499 GOCART simulations. *J. Geophys. Res.*, **118**, 1–15, doi:10.1029/2012JD018294.

500 Su, W., N. G. Loeb, K. Xu, G. L. Schuster, and Z. A. Eitzen, 2010b: An estimate of aerosol
501 indirect effect from satellite measurements with concurrent meteorological analysis. *J.*
502 *Geophys. Res.*, **115** (D18219), D18 219, doi:10.1029/2010JD013948.

503 Trenberth, K. E., J. T. Fasullo, and J. Kiehl, 2009: Earth’s global energy budget. *Bull. Am.*
504 *Meteor. Soc.*, **90**, 311–323, doi:10.1175/2008BAMS2634.1.

505 Trepte, Q. Z., P. Minnis, C. Trepte, and S. Sun-Mack, 2010: Improved cloud detections in
506 CERES Edition 3 algorithm and comparison with the CALIPSO vertical feature mask.
507 *13th Conference on Atmospheric Radiation*, Am. Meteorol. Soc., Oregon, Portland.

508 Wang, H. and W. Su, 2013: Evaluating and understanding top of the atmosphere cloud
509 radiative effects in Intergovernmental Panel on Climate Change (IPCC) fifth assessment
510 report (AR5) coupled model intercomparison project phase 5 (CMIP5) models using
511 satellite observations. *J. Geophys. Res.*, **118**, 1–17, doi:10.1029/2012JD018619.

- 512 Wielicki, B. A., B. R. Barkstrom, E. F. Harrison, R. B. Lee, G. L. Smith, and J. E. Cooper,
513 1996: Clouds and the Earth's Radiant Energy System (CERES): An Earth Observing
514 System experiment. *Bull. Amer. Meteor. Soc.*, **77**, 853–868.
- 515 Wild, M., D. Folini, C. Schar, N. G. Loeb, E. G. Dutton, and G. Konig-Langlo, 2013:
516 The global energy balance from a surface perspective. *Clim. Dyn.*, **40**, 3107–3134, doi:
517 10.1007/s00382-012-1569-8.
- 518 Zhang, J., S. A. Christopher, L. A. Remer, and Y. J. Kaufman, 2005: Shortwave aerosol
519 radiative forcing over cloud-free oceans from Terra: 2. Seasonal and global distributions.
520 *J. Geophys. Res.*, **110 (D10S24)**, D10S24, doi:10.1029/2004JD005009.

521 **List of Tables**

- 522 1 Comparison of CERES-Aqua and CERES-NPP measured SW, daytime LW,
523 and nighttime LW radiances ($\text{Wm}^{-2}\text{sr}^{-1}$) and fluxes (Wm^{-2}) using matched
524 footprints of 2013 and 2014.

24

TABLE 1. Comparison of CERES-Aqua and CERES-NPP measured SW, daytime LW, and nighttime LW radiances ($\text{Wm}^{-2}\text{sr}^{-1}$) and fluxes (Wm^{-2}) using matched footprints of 2013 and 2014.

	SW	Daytime LW	Nighttime LW
Sample Number	147894	192178	187880
Mean CERES-Aqua Radiance	68.1	77.4	74.4
Mean CERES-NPP Radiance	69.2	77.0	74.3
Radiance RMS Error	4.1	1.6	0.8
Mean CERES-Aqua Flux	230.1	235.7	226.4
Mean CERES-NPP Flux	233.9	234.7	226.1
Flux RMS Error	14.6	5.0	3.1

525 List of Figures

- 526 1 Radiance comparisons between matched CERES-Aqua and CERES-NPP foot-
527 prints, (a) SW; (b) daytime LW; and (c) nighttime LW using data of 2013 and
528 2014. The total number of footprints, the mean radiances, and the radiance
529 RMS errors are summarized in Table 1. 27
- 530 2 Flux comparisons between matched CERES-Aqua and CERES-NPP foot-
531 prints, (a) SW; (b) daytime LW; and (c) nighttime LW using data of 2013
532 and 2014. The total number of footprints, the mean fluxes, and the flux RMS
533 errors are summarized in Table 1. 28
- 534 3 Monthly mean insolation difference (Wm^{-2}) between CERES-NPP and CERES-
535 Aqua (NPP-Aqua) for April 2013. 29
- 536 4 Monthly mean a) TOA reflected SW flux difference between CERES-NPP and
537 CERES-Aqua (NPP-Aqua), and b) albedo difference between CERES-NPP
538 and CERES-Aqua (NPP-Aqua) for April 2013. 30
- 539 5 Cloud fraction (a) and cloud optical depth (b) differences between VIIRS and
540 MODIS (VIIRS-MODIS) retrievals for April 2013. 31
- 541 6 Schematic diagram of convoluting the MODIS pixels into the simulated Aqua
542 and NPP footprints. Left depicts the processes involved in producing the
543 simulated Aqua footprints; middle for simulated NPP footprints with MODIS
544 retrievals; and right for simulated NPP footprints with VIIRS-like retrievals. 32
- 545 7 The gridded monthly mean TOA instantaneous SW fluxes from the simulated
546 Aqua footprints (F_a^s , a), the flux differences caused by footprint size difference
547 between simulated NPP and simulated Aqua ($F_n^s - F_a^s$, b), and the flux differ-
548 ences caused by both footprint size and cloud property differences ($F_n'^s - F_a^s$,
549 c) using April 2013 data. Regions shown in white have large sample number
550 differences between simulated Aqua and simulated NPP. 33

- 551 8 The gridded monthly mean TOA daytime LW fluxes from the simulated Aqua
552 footprints (F_a^s , a), the flux differences caused by footprint size difference be-
553 tween simulated NPP and simulated Aqua ($F_n^s - F_a^s$, b), and the flux differ-
554 ences caused by both footprint size and cloud property differences ($F_n'^s - F_a^s$,
555 c) using April 2013 data. Regions shown in white have large sample number
556 differences between simulated Aqua and simulated NPP. 34
- 557 9 The gridded monthly mean TOA nighttime LW fluxes from the simulated
558 Aqua footprints (F_a^s , a), the flux differences caused by footprint size difference
559 between simulated NPP and simulated Aqua ($F_n^s - F_a^s$, b), and the flux differ-
560 ences caused by both footprint size and cloud property differences ($F_n'^s - F_a^s$,
561 c) using April 2013 data. Regions shown in white have large sample number
562 differences between simulated Aqua and simulated NPP. 35

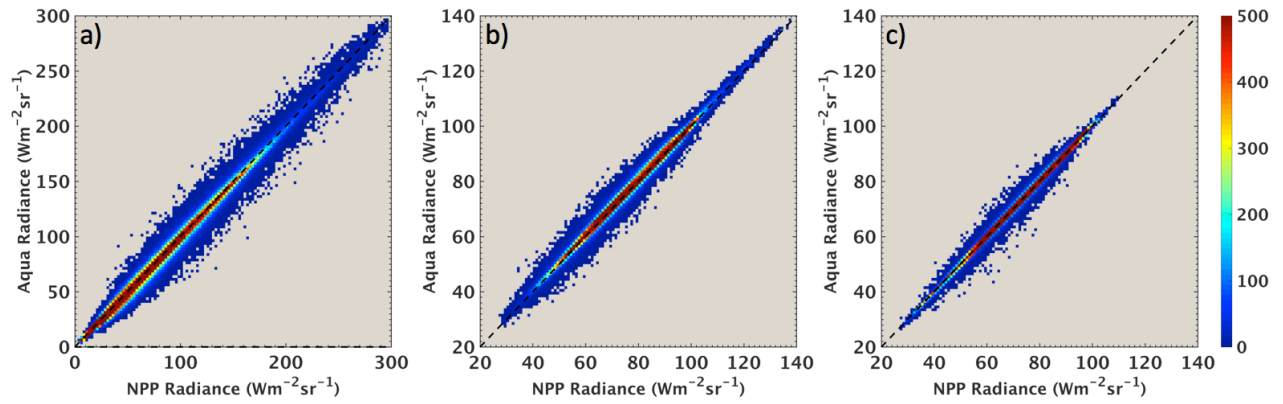


FIG. 1. Radiance comparisons between matched CERES-Aqua and CERES-NPP footprints, (a) SW; (b) daytime LW; and (c) nighttime LW using data of 2013 and 2014. The total number of footprints, the mean radiances, and the radiance RMS errors are summarized in Table 1.

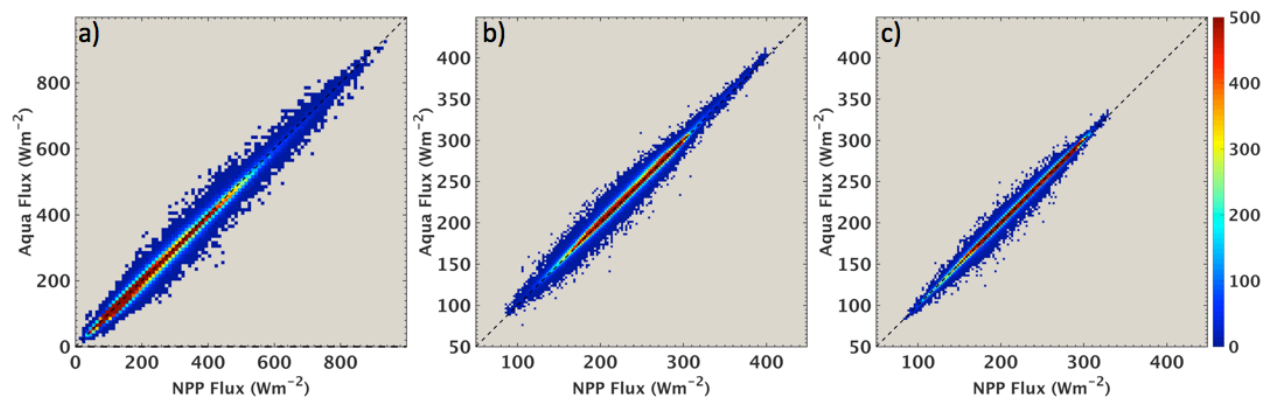


FIG. 2. Flux comparisons between matched CERES-Aqua and CERES-NPP footprints, (a) SW; (b) daytime LW; and (c) nighttime LW using data of 2013 and 2014. The total number of footprints, the mean fluxes, and the flux RMS errors are summarized in Table 1.

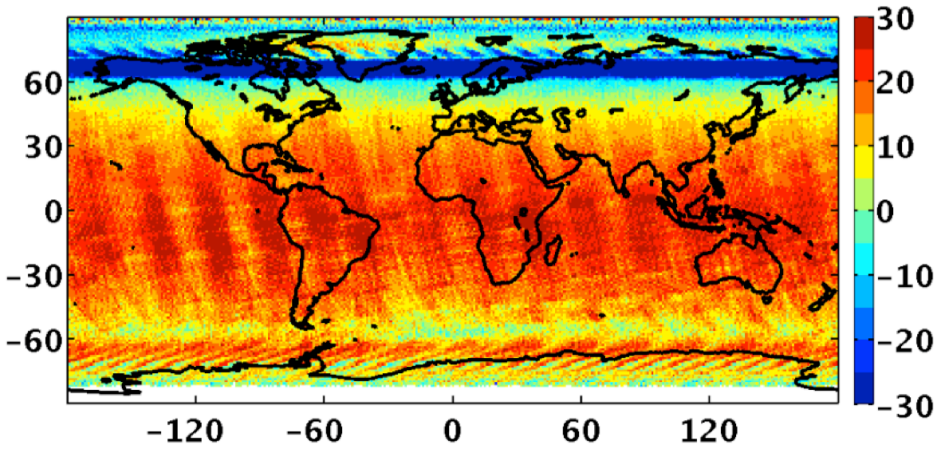


FIG. 3. Monthly mean insolation difference (Wm^{-2}) between CERES-NPP and CERES-Aqua (NPP-Aqua) for April 2013.

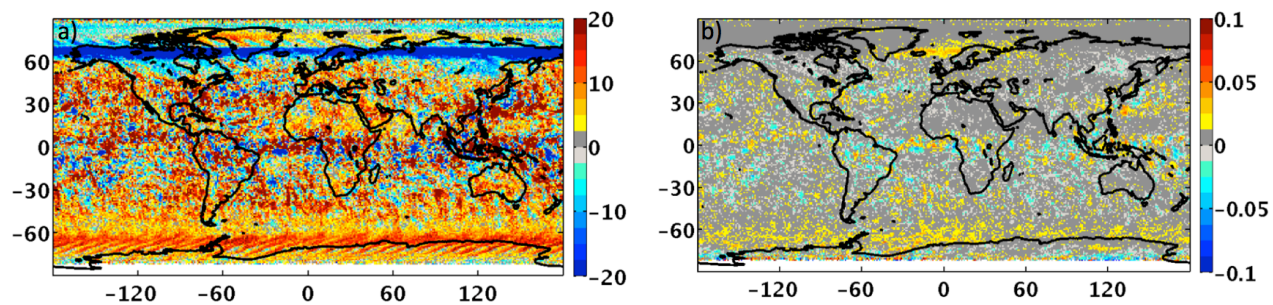


FIG. 4. Monthly mean a) TOA reflected SW flux difference between CERES-NPP and CERES-Aqua (NPP-Aqua), and b) albedo difference between CERES-NPP and CERES-Aqua (NPP-Aqua) for April 2013.

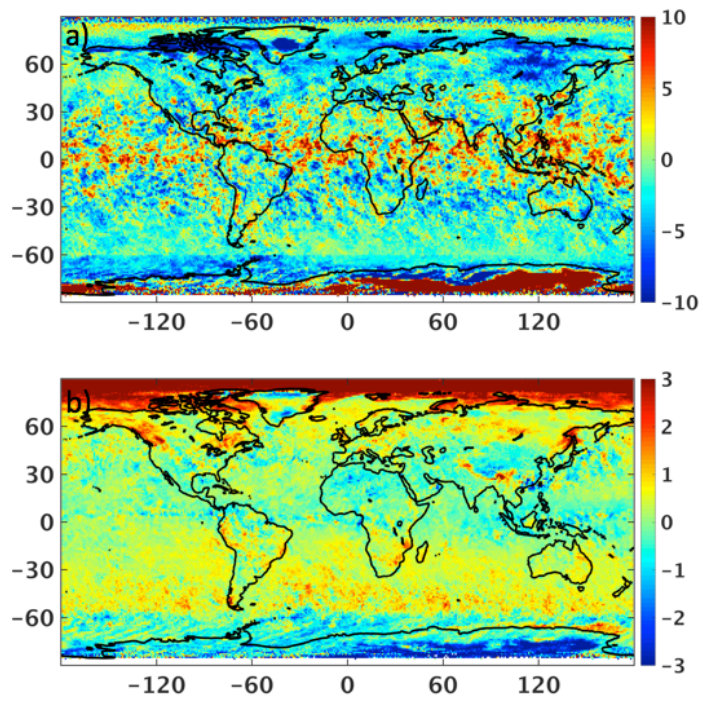


FIG. 5. Cloud fraction (a) and cloud optical depth (b) differences between VIIRS and MODIS (VIIRS-MODIS) retrievals for April 2013.

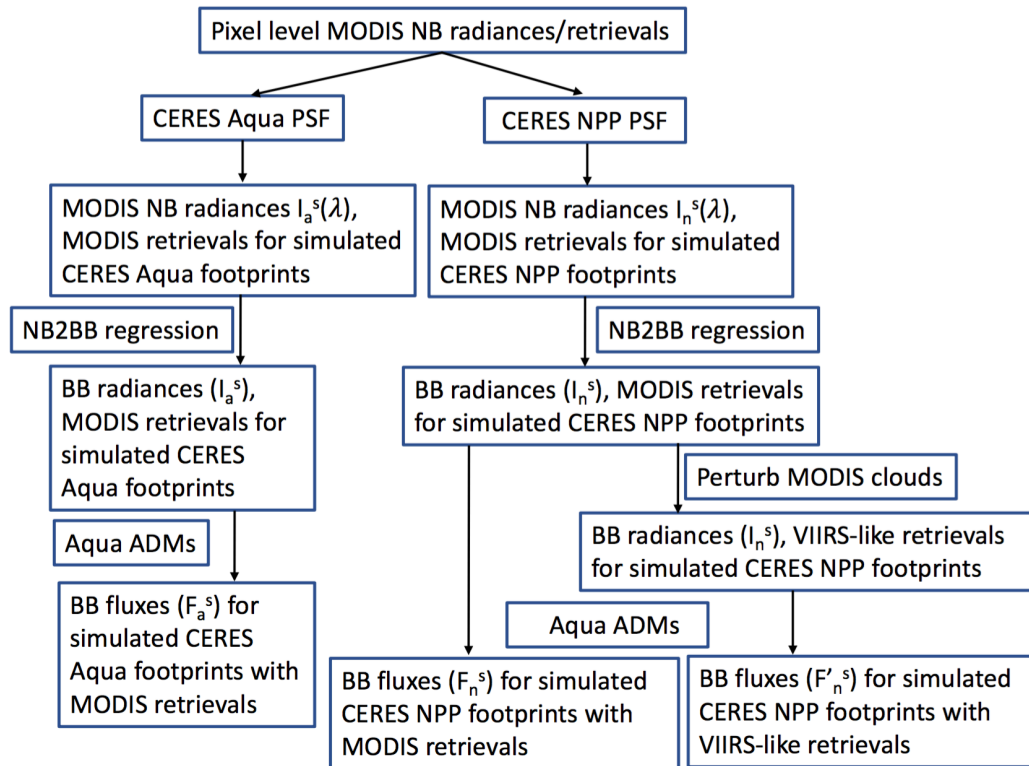


FIG. 6. Schematic diagram of convoluting the MODIS pixels into the simulated Aqua and NPP footprints. Left depicts the processes involved in producing the simulated Aqua footprints; middle for simulated NPP footprints with MODIS retrievals; and right for simulated NPP footprints with VIIRS-like retrievals.

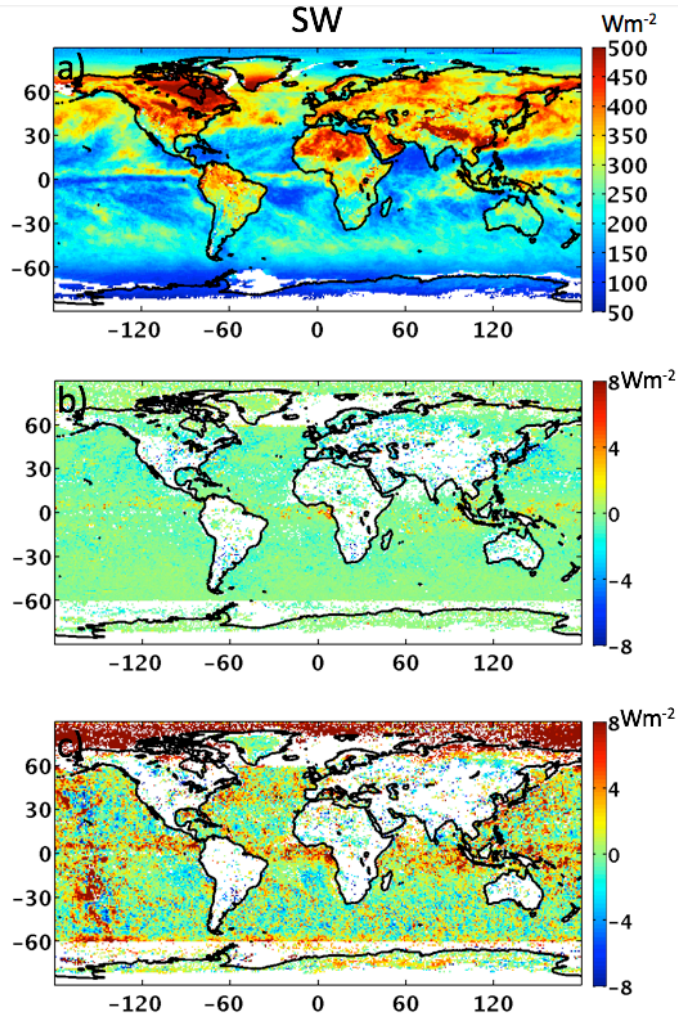


FIG. 7. The gridded monthly mean TOA instantaneous SW fluxes from the simulated Aqua footprints (F_a^s , a), the flux differences caused by footprint size difference between simulated NPP and simulated Aqua ($F_n^s - F_a^s$, b), and the flux differences caused by both footprint size and cloud property differences ($F_n'^s - F_a^s$, c) using April 2013 data. Regions shown in white have large sample number differences between simulated Aqua and simulated NPP.

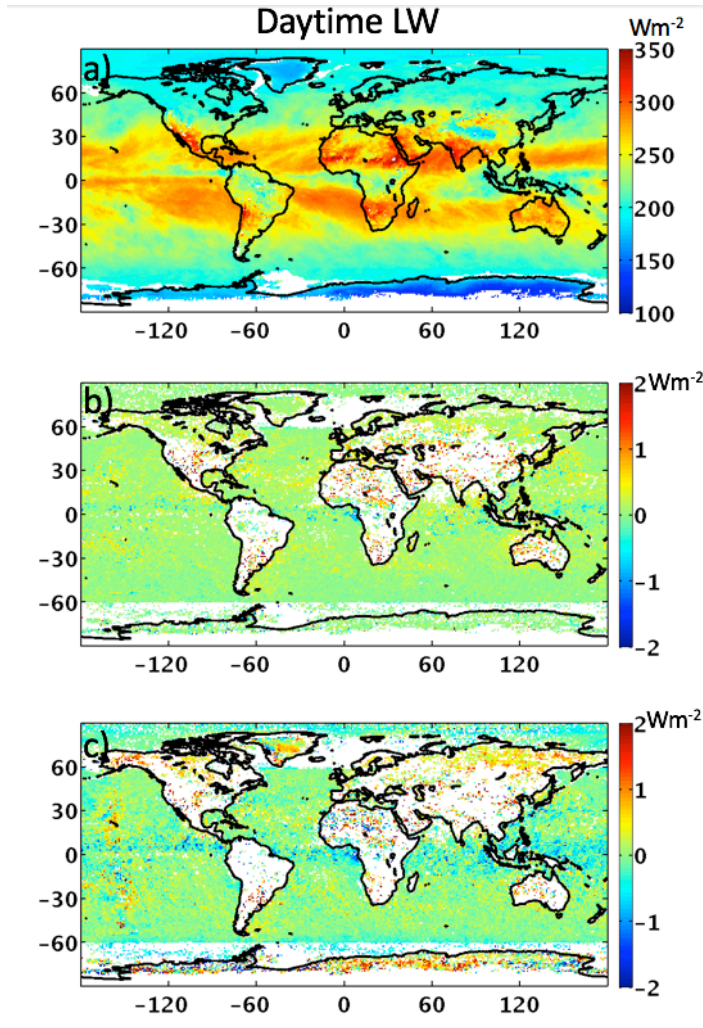


FIG. 8. The gridded monthly mean TOA daytime LW fluxes from the simulated Aqua footprints (F_a^s , a), the flux differences caused by footprint size difference between simulated NPP and simulated Aqua ($F_n^s - F_a^s$, b), and the flux differences caused by both footprint size and cloud property differences ($F_n'^s - F_a^s$, c) using April 2013 data. Regions shown in white have large sample number differences between simulated Aqua and simulated NPP.

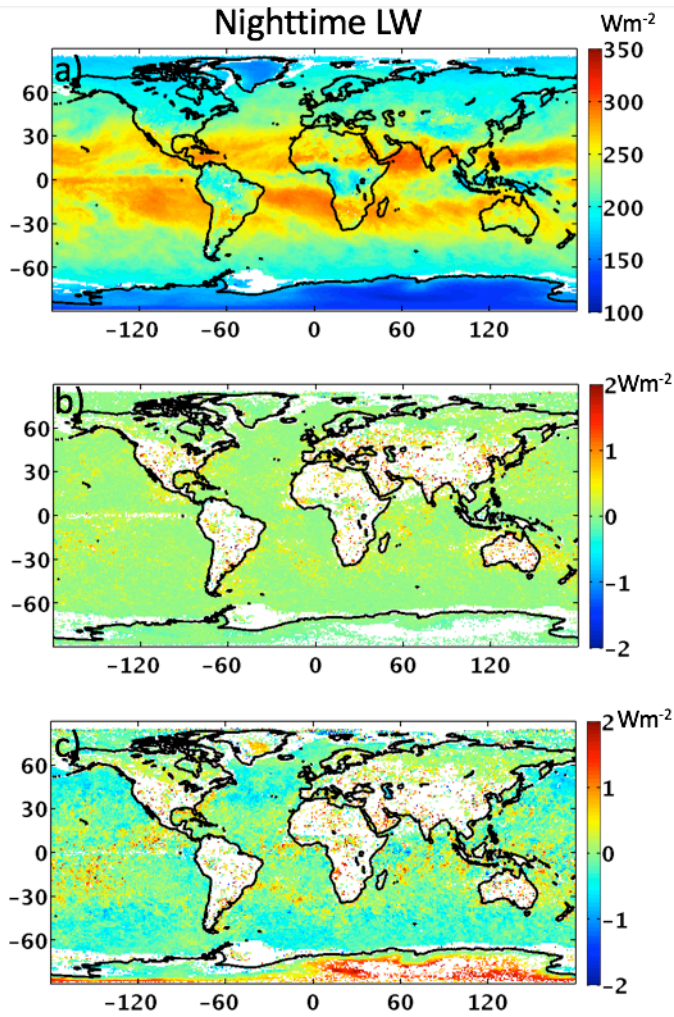


FIG. 9. The gridded monthly mean TOA nighttime LW fluxes from the simulated Aqua footprints (F_a^s , a), the flux differences caused by footprint size difference between simulated NPP and simulated Aqua ($F_n^s - F_a^s$, b), and the flux differences caused by both footprint size and cloud property differences ($F_n'^s - F_a^s$, c) using April 2013 data. Regions shown in white have large sample number differences between simulated Aqua and simulated NPP.